

# Pair modes of organic cations in hybrid perovskites: Insight from first-principles calculations of supercell models

Jingrui Li,<sup>1,\*</sup> Jari Järvi,<sup>1,2</sup> and Patrick Rinke<sup>1</sup>

<sup>1</sup>*Centre of Excellence in Computational Nanoscience (COMP) and Department of Applied Physics, Aalto University, P.O.Box 11100, FI-00076 AALTO, Finland*

<sup>2</sup>*Department of Physics, University of Helsinki, P.O.Box 64, FI-00014 University of Helsinki, Finland*

We have studied the properties of the prototype hybrid organic-inorganic perovskite  $\text{CH}_3\text{NH}_3\text{PbI}_3$  using relativistic density functional theory (DFT). For our analysis we introduce the concept of  $\text{CH}_3\text{NH}_3^+$  “pair modes”, that is, characteristic relative orientations of two neighboring  $\text{CH}_3\text{NH}_3^+$  cations. In our previous work [Phys. Rev. B **94**, 045201 (2016)] we identified two preferential orientations that a single  $\text{CH}_3\text{NH}_3^+$  cation adopts in a unit cell. The total number of relevant pairs can be reduced from the resulting 196 combinations to only 25 by applying symmetry operations. DFT results of several  $2 \times 2 \times 2$  supercell models reveal the dependence of the total energy, band gap and band structure on the distribution of  $\text{CH}_3\text{NH}_3^+$  cations and the pair modes. We have then analyzed the pair-mode distribution of a series of  $3 \times 3 \times 3$  supercell models with disordered  $\text{CH}_3\text{NH}_3^+$  cations. Our results show that diagonally-oriented  $\text{CH}_3\text{NH}_3^+$  cations are rare in optimized  $\text{CH}_3\text{NH}_3\text{PbI}_3$  supercell structures. The prevailing pair modes are advantageous for the formation of linear domains. Our pair-mode concept provides combined atomistic-statistical insight to understand the disordered structures in bulk hybrid perovskite materials.

PACS numbers: 61.50.Ah, 71.15.Mb, 71.15.Nc, 81.07.Pr

## I. INTRODUCTION

Hybrid perovskite photovoltaic (HPPV) technology [1,2] is the most recent rising star in the emerging solar-cell community due to its record increase in power-conversion efficiency (PCE) during the last four years [3]. The current state-of-the-art HPPV architecture was proposed in 2012 achieving  $\sim 10\%$  PCE [4,5]. Now the PCE of HPPV cells has already reached 22%, overtaking the best-performing inorganic-based single-junction thin-film cells such as CdTe and copper-indium-gallium-selenide (CIGS) cells [3,6]. The most common photoactive material in HPPV cells is methylammonium ( $\text{MA} \equiv \text{CH}_3\text{NH}_3$ ) lead triiodide ( $\text{CH}_3\text{NH}_3\text{PbI}_3$ , shortened as  $\text{MAPbI}_3$  hereafter). This hybrid perovskite material exhibits several advantageous features for photovoltaic applications, such as a band gap close to the optimal value for single-junction solar-cell absorbers [7], excellent absorption strength in the visible part of the solar spectrum [8], and high mobilities for both electron and hole transport [9,10]. It can be synthesized in solution at low temperature from common starting materials that have limited harm to the environment. Therefore HPPV cells are considered as promising candidates that can offer clean, affordable and sustainable energy.

Apart from the PCE improvement, recent experimental and theoretical studies in HPPV technology have focused on the origin of the high mobility and low recombination rate [9–12], the observed current-voltage hysteresis [7,13–15], and the stability of hybrid perovskites materials [16–18]. To resolve open questions in hybrid perovskites it is imperative to develop a comprehensive understanding of their atomic structure, which is both fundamental and challenging due to the structure’s complexity. Taking the prototype hybrid perovskite  $\text{MAPbI}_3$  as an example, the central cation  $\text{MA}^+$  is

not spherical (as, e.g.,  $\text{Cs}^+$  in the conventional perovskite  $\text{CsSnI}_3$ ) but exhibits polarity and an orientational preference in the lattice. At low temperatures,  $\text{MAPbI}_3$  assumes a minimal-energy structure with regularly-aligned  $\text{MA}^+$  cations and thereby a regularly-deformed inorganic  $\text{PbI}_3^-$  matrix, resulting in an orthorhombic phase. Conversely, at room temperature or above, the  $\text{MA}^+$  cations are randomly oriented due to thermal fluctuations, forming (dynamically-)disordered structures [7,19–21]. Experimental [22,23] and theoretical [23–25] studies suggest that the activation energy for the reorientation of the C–N bond is of the order of 100 meV (corresponding to a characteristic thermal energy of  $\sim 1200$  K). The  $\text{MA}^+$  ions therefore do not rotate freely at  $< 400$  K, but are bound to the inorganic framework by hydrogen bonds [27]. They form localized patterns [28–30] on a small length scale, which makes  $\text{MAPbI}_3$  appear effectively cubic.

Modeling the orientational disorder of  $\text{MA}^+$  ions in  $\text{MAPbI}_3$  is a challenging task. Quantum mechanical first principles techniques are required to correctly describe the hydrogen bonding of  $\text{MA}^+$  ions to the inorganic cage and the corresponding distortions of the cage. However, even density-functional theory (DFT), which in local or semi-local approximations is currently the most computationally efficient first principles technique, cannot scale up to the required length scales or the large number of candidate structures. The simple primitive-cell model is not representative of  $\text{MAPbI}_3$ ’s atomic structure, as it effectively describes a system of infinitely many aligned polar  $\text{MA}^+$  ions. The dipole introduced by each  $\text{MA}^+$  unit can be canceled by compensating alignments of  $\text{MA}^+$  ions in an appropriately chosen supercell model. For such compensated models, the atomic and electronic structure, especially in the low-temperature orthorhombic and tetragonal phases, can then be calculated at the DFT or beyond level by means of small supercell models such as  $\sqrt{2} \times \sqrt{2} \times 2$  and  $2 \times 2 \times 2$  [23,31–34].  $2 \times 2 \times 2$  supercell models have also been adopted to study the distribution of  $\text{MA}^+$  ori-

\* jingrui.li@aalto.fi

entations at a finite temperature using *ab initio* molecular dynamics (MD) [29,35]. However, to really model disorder we would need to know the structure of MAPbI<sub>3</sub> on a length scale of a few to a few tens of single (primitive) cells.  $2 \times 2 \times 2$  supercell models do not suffice for this purpose because of the periodic boundary conditions, while DFT calculations for larger supercell models become computationally very demanding. To our knowledge, the application of DFT to large MAPbI<sub>3</sub> supercells has mostly been limited to defect modeling [36,37]. Disordered structures, such as the behavior of domains has so far only been investigated with classical Monte Carlo simulations [29,30].

In our previous work [27], we have comprehensively analyzed the atomic structure of hybrid perovskites using the primitive-cell model. We found several stable locations of MA<sup>+</sup> in the lattice. Moreover, our analysis revealed that the stability of hybrid perovskites is closely related to the deformation of the inorganic cage, which acts synergetically with the organic ions analogous to a chicken-and-egg paradox. In this work, we performed DFT calculations for a number of different MAPbI<sub>3</sub> supercell models and focus on the pairs of neighboring MA<sup>+</sup> ions. We devised a pair-mode description that reduces each MA<sup>+</sup> ion to a dipole [38] with discrete orientations that were adopted from our previous primitive-cell results [27]. We then defined the relative geometry of two nearest individual dipoles as a “pair mode”. With the pair-mode concept, we were then able to relate the dependence of certain MAPbI<sub>3</sub> properties (e.g., total energy, band structure) to the distribution of MA<sup>+</sup>-orientations and to the dipoles’ alignment. This was done by studying a series of  $2 \times 2 \times 2$  supercell models. We further investigated  $3 \times 3 \times 3$  supercell models focusing on the distribution of pair modes. This distribution tells us for a given dipole which dipole-orientations are preferred in its surrounding, thus providing knowledge of the local structure beyond a single MAPbI<sub>3</sub> unit cell. The atomic structure of the pair modes, as the physical origin of this pair-mode distribution, will be discussed in detail in a forthcoming paper [39].

The remainder of this paper is organized as follows. In Sec. II, we briefly describe the model systems and the computational details of our DFT calculations. Section III outlines the concept of pair modes, and uses this concept to discuss the results of the supercell models. Finally, Sec. IV concludes with a summary.

## II. COMPUTATIONAL DETAILS

The supercell models considered in this paper were constructed based on single (primitive) cells. In each single cell, the MA<sup>+</sup> is located close to the centre of the cell, Pb<sup>2+</sup> at the corners, and I<sup>-</sup> at the edge-centers. We considered a series of  $2 \times 2 \times 2$  and  $3 \times 3 \times 3$  supercell models for different purposes. In  $2 \times 2 \times 2$  supercell models the total dipole moment can be easily canceled with regular alignments of MA<sup>+</sup> ions. Although a  $2 \times 2 \times 2$  supercell model is larger than  $a\sqrt{2} \times a\sqrt{2} \times 1$  model, it has the advantage that it does not introduce artificial differences between the three lattice directions *a priori*.

Compared with the  $2 \times 2 \times 2$  counterparts, the larger  $3 \times 3 \times 3$  supercell models contain more MA<sup>+</sup> cations, thus providing appropriate model systems to mimic the disordered structures by introducing randomly oriented MA<sup>+</sup> ions. The considered supercell models were initialized with different MA<sup>+</sup> alignments.

In our previous study [27] we demonstrated that the “PBE+vdW” exchange-correlation functional produces the lattice constants of hybrid perovskite systems in good agreement with experiment, and can properly describe the interaction between the organic cations and the inorganic framework. Thus we adopted this functional for all DFT calculations in this work. Specifically, the Perdew-Burke-Ernzerhof (PBE) generalized gradient approximation [40] was used as the exchange-correlation functional, and the long-range van der Waals (vdW) interactions were described by employing the Tkatchenko-Scheffler method based on the Hirshfeld partitioning of the electron density [41]. In addition, scalar relativistic effects were included via the zero-order regular approximation (ZORA) [42]. Although spin-orbit coupling [43–46] and exact exchange or many-body corrections [45,47,48] have significant impact on the band structure of MAPbI<sub>3</sub>, we did not include them in the band-structure calculations (for the  $2 \times 2 \times 2$  supercell models), since they are computationally very demanding. For the relative differences of band gaps between different supercell models PBE+vdW+ZORA is sufficient.

All calculations were carried out using the all-electron numeric-atom-centered orbital code FHI-AIMS [49–51]. For the  $2 \times 2 \times 2$  supercell models, we used a  $\Gamma$ -centered  $4 \times 4 \times 4$  *k*-point mesh and tier 2 basis sets for both structure relaxation and band-structure calculations. We performed direct lattice-vector optimization with the analytical stress tensor implemented in FHI-AIMS [52]. For the larger  $3 \times 3 \times 3$  supercells, we have reduced the computational expense by employing a  $2 \times 2 \times 2$  *k*-point mesh and tier 1 basis sets. The geometries were optimized for a fixed size of the cubic unit cell, for which the lattice parameter  $a = 18.94$  Å was adopted based on the experimental value  $a_0 = 6.31$  Å of the primitive cell [7]. The results of all relevant calculations of this work are available from the Novel Materials Discovery (NoMaD) repository [53].

## III. RESULTS AND DISCUSSIONS

### A. Definition of CH<sub>3</sub>NH<sub>3</sub><sup>+</sup> “pair modes”

The essential difference between conventional perovskites such as CsPbI<sub>3</sub> and hybrid perovskites is the monovalent central cation. Metal cations such as Cs<sup>+</sup> are spherically symmetric, while the polar organic CH<sub>3</sub>NH<sub>3</sub><sup>+</sup> cation has a permanent dipole moment pointing from the C-end (the methyl group) to the N-end (the ammonium cation group). Thus, in a primitive-cell model all MA<sup>+</sup> ions will be aligned parallel. This would result in a large dipole moment in the bulk material, which is not observed experimentally. Supercell models allow us to cancel the total dipole moment in the supercell. In this paper, we calculated the total dipole moment within a supercell by the vector sum of individual MA<sup>+</sup> dipole moments

(or its average per  $\text{MAPbI}_3$  unit) and represent it in terms of  $p_0$ , the permanent dipole moment of an isolate  $\text{MA}^+$  in vacuum. Our PBE+vdW/tier 2 result of  $p_0$  is 2.2 D, very close to the B3LYP/6-31G\* result of 2.3 D [28].

Our previous DFT calculations [27] revealed two stable structures of the cubic primitive-cell model, as shown in Fig. 1(a). Specifically, in the left structure of Fig. 1(a), the C–N bond is oriented along the diagonal ([111] or equivalent) direction of the single unit cell, while in the right structure it is oriented along the face-to-face ([100] or equivalent) direction with a small deviation. The face-to-face  $\text{MA}^+$  structure is 21 meV more stable than the diagonal structure. We attribute this stability to the considerably larger deformation of the inorganic-framework in the face-to-face structure. As a side note, the internal atomic geometry of  $\text{MA}^+$  in  $\text{MAPbI}_3$  is nearly independent of its location in the unit cell.

To simplify our notation, we abstract each  $\text{MA}^+$  in the optimized  $\text{MAPbI}_3$  structure by an arrow along its C–N bond that represents its dipole moment. Corresponding to the 8 diagonal and 6 face-to-face directions in the cubic single cell, there are altogether 14 possible directions for such a dipole. They are illustrated in Figs. 1(b) and (c), respectively.

In our definition, a “pair mode” is the alignment of a pair of neighboring  $\text{MA}^+$  ions. From the 14 dipole directions shown in Fig. 1 we can derive  $14^2 = 196$  pair modes. However, this number can be significantly reduced to 25 by considering only symmetry inequivalent modes, since many modes can be transformed into each other. The 25 inequivalent modes are listed in Fig. 2. Figure 3 shows an example of transformations among several equivalent modes. We will discuss our supercell models in terms of the pair modes listed in Fig. 2 hereafter. Specifically, modes No. 1–6 and No. 11–13 are constructed by two diagonal dipoles, modes No. 7–10 and No. 14–17 by one diagonal and one face-to-face dipole, and modes No. 18–25 by two face-to-face dipoles. In this paper we will only discuss dipoles with “strict” face-to-face orientations. Pair modes resulting from dipoles that deviate from the face-to-face line by the angle found in our previous work [27] are presented in Sec. S1 of Ref. [54].

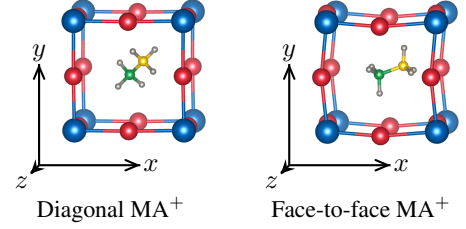
## B. Properties of optimized $2 \times 2 \times 2$ supercell models

### 1. General properties analysis based on dipole-direction distribution

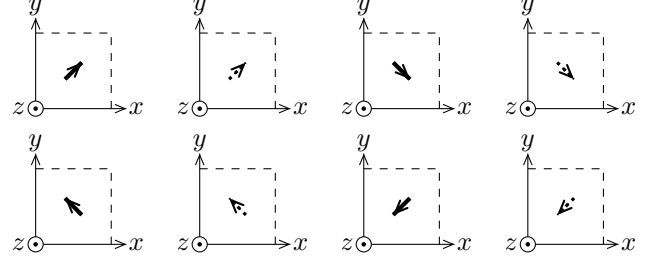
In our previous primitive-cell study we found only two stable structures [27], as alluded to before. For  $2 \times 2 \times 2$  supercell models, the situation changes dramatically. There are many possible alignments of  $\text{MA}^+$  dipoles in the initial structures. The optimization of them using the aforementioned DFT approach results in different atomic geometries corresponding to different local total-energy minima. Here we first select from the many local minima and structures that we found the nonpolar structures, in which the vector sum of  $\text{MA}^+$  dipole moments (approximately) vanishes.

Figure 4 shows a geometry optimized  $2 \times 2 \times 2$  supercell in which all  $\text{MA}^+$  ions are oriented diagonally. The C–N bonds

(a) Two stable orientations of  $\text{MA}^+$  in the primitive-cell model



(b) Possible directions of a diagonal  $\text{MA}^+$  dipole



(c) Possible directions of a face-to-face  $\text{MA}^+$  dipole

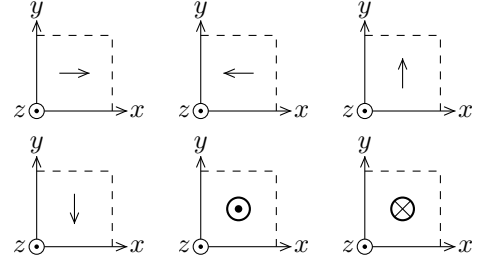


Figure 1. Symbolic representation of a  $\text{CH}_3\text{NH}_3^+$  ion by an arrow pointing from C to N. (a) Two stable structures (left: with diagonally-oriented  $\text{MA}^+$ , and right: with  $\text{MA}^+$  oriented approximately along face-to-face) obtained from primitive-cell calculations (data taken from Ref. [27]). C, N, H, Pb and I atoms are colored in green, yellow, gray, blue and red, respectively. (b,c) Dipole representation for  $\text{MA}^+$  along (b) diagonal and (c) face-to-face orientations.  $\odot$  and  $\otimes$  indicate dipoles that are perpendicular to the plane of the paper and point out of and into it, respectively. Likewise, thick solid arrows in panel (b) point out of the plane of the paper, while dashed arrows point into the paper.

are aligned parallel and alternately point in opposite directions. This results in a nearly-vanishing net dipole moment in the supercell: the three components of the average dipole-moment vector are 0.001, 0.004 and 0.003  $p_0$ .

Figure 5 shows four optimized  $2 \times 2 \times 2$  supercells, in which all  $\text{MA}^+$  cations are oriented face-to-face. Also shown are their band structures along three high-symmetry lines  $\Gamma$ –X,  $\Gamma$ –Y and  $\Gamma$ –Z around the band gap (for band structures along more high-symmetry lines we refer to Sec. S2 of Ref. [54]). Corresponding key parameters of these structures (e.g., relative stability, band gap) are listed in Table I. Structure III [Fig. 5(c)] is the most stable one as it corresponds to the lowest total energy among them. We set its total energy to 0 hereafter. The total energy of structures I [Fig. 5(a)], II [Fig. 5(b)] and IV [Fig. 5(d)] are 898, 182 and 500 meV per unit cell, or

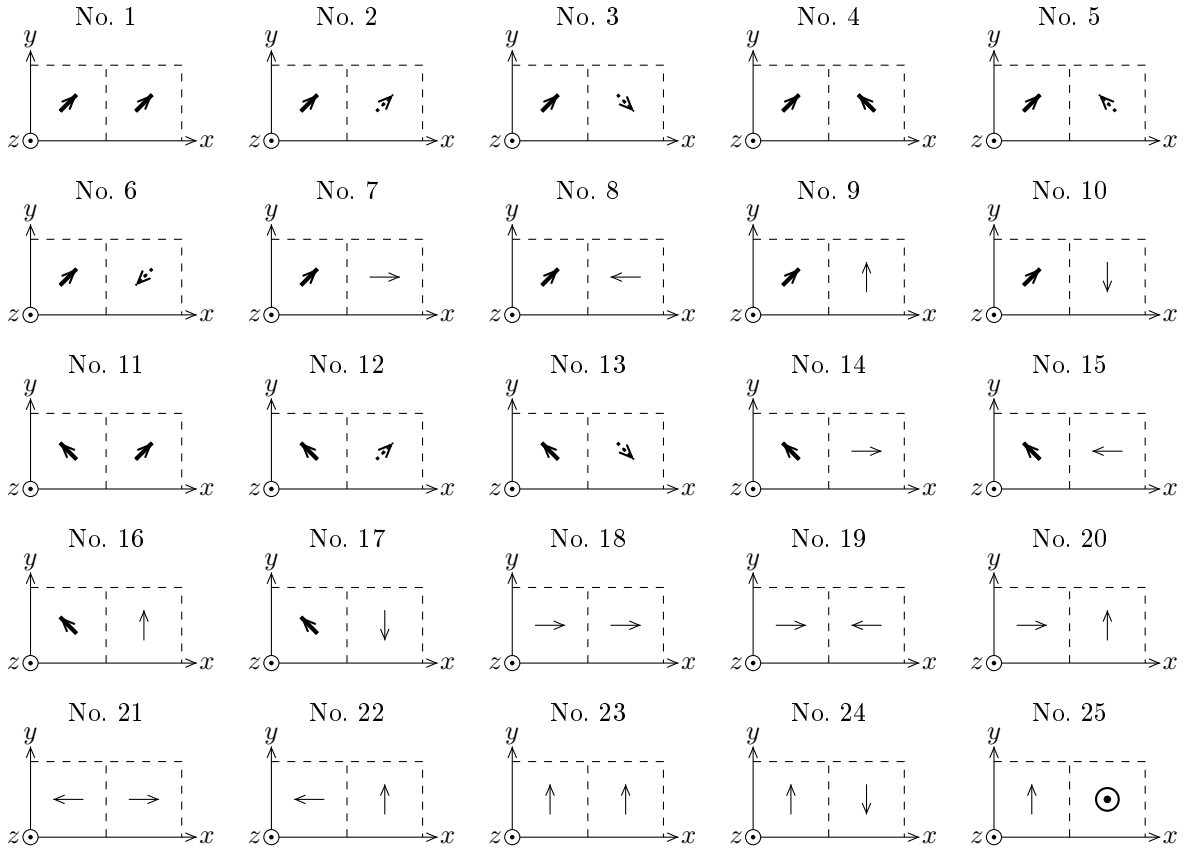


Figure 2. The 25 pair modes of neighboring  $\text{MA}^+$  ions considered in this paper. Each  $\text{MA}^+$  ion is represented by arrows indicating the direction from C to N, that is, the direction of the  $\text{CH}_3\text{NH}_3^+$  dipole.

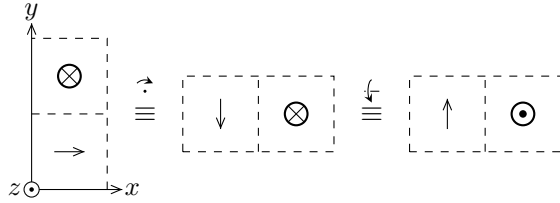


Figure 3. An arbitrary pair mode (left) being equivalent to mode No. 25 (right) listed in Fig. 2 via a series of symmetry operations: rotation around  $-z$  for  $90^\circ$  then rotation around  $x$  for  $180^\circ$ .

112, 23 and 63 meV per  $\text{MAPbI}_3$ , respectively. The total energy of the structure shown in Fig. 4 is 170 meV per  $\text{MAPbI}_3$ , much higher than structures I–IV. Following the analysis of our previous work [27], this can be rationalized by the occurrence of diagonally-oriented  $\text{MA}^+$  ions. These diagonally oriented dipoles prevent the inorganic framework from releasing energy by deforming the inorganic cage, which leads to a significantly higher total energy. It is thus unlikely that many diagonally oriented dipoles occur in  $\text{MAPbI}_3$ , which is also confirmed by our supercell calculations. Therefore we only focus on structures I–IV hereafter, in which only face-to-face  $\text{MA}^+$  ions are involved. Some structural parameters and the band structure of the systems shown in Fig. 4 are given in

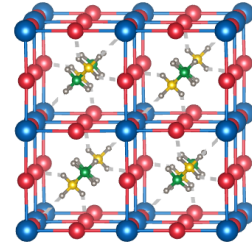


Figure 4. An optimized  $2 \times 2 \times 2$  supercell structure in which all  $\text{MA}^+$  cations are oriented diagonally. The hydrogen bonds between  $\text{I}^-$  anions and H atoms in the  $-\text{NH}_3^+$  group are highlighted by gray dashed lines.

Sec. S3 of Ref. [54].

For each optimized supercell structure, we illustrate the  $\text{MA}^+$ -alignment “pattern” in both Fig. 5 and Table I. These patterns show that in structures I–III the  $\text{MA}^+$  cations are (approximately) located within the  $xy$  plane and regularly aligned. For the properties of each of these system, we therefore observe an equivalence between the  $x$  and  $y$  directions, whereas the  $z$ -direction exhibits differences. For example, the lattice parameters  $a$  and  $b$  are approximately equal, whereas  $c$  differs (cf. Table I). This equivalence is also reflected in the band structures [see Figs. 5(a)–(c), upper-right panels]: for

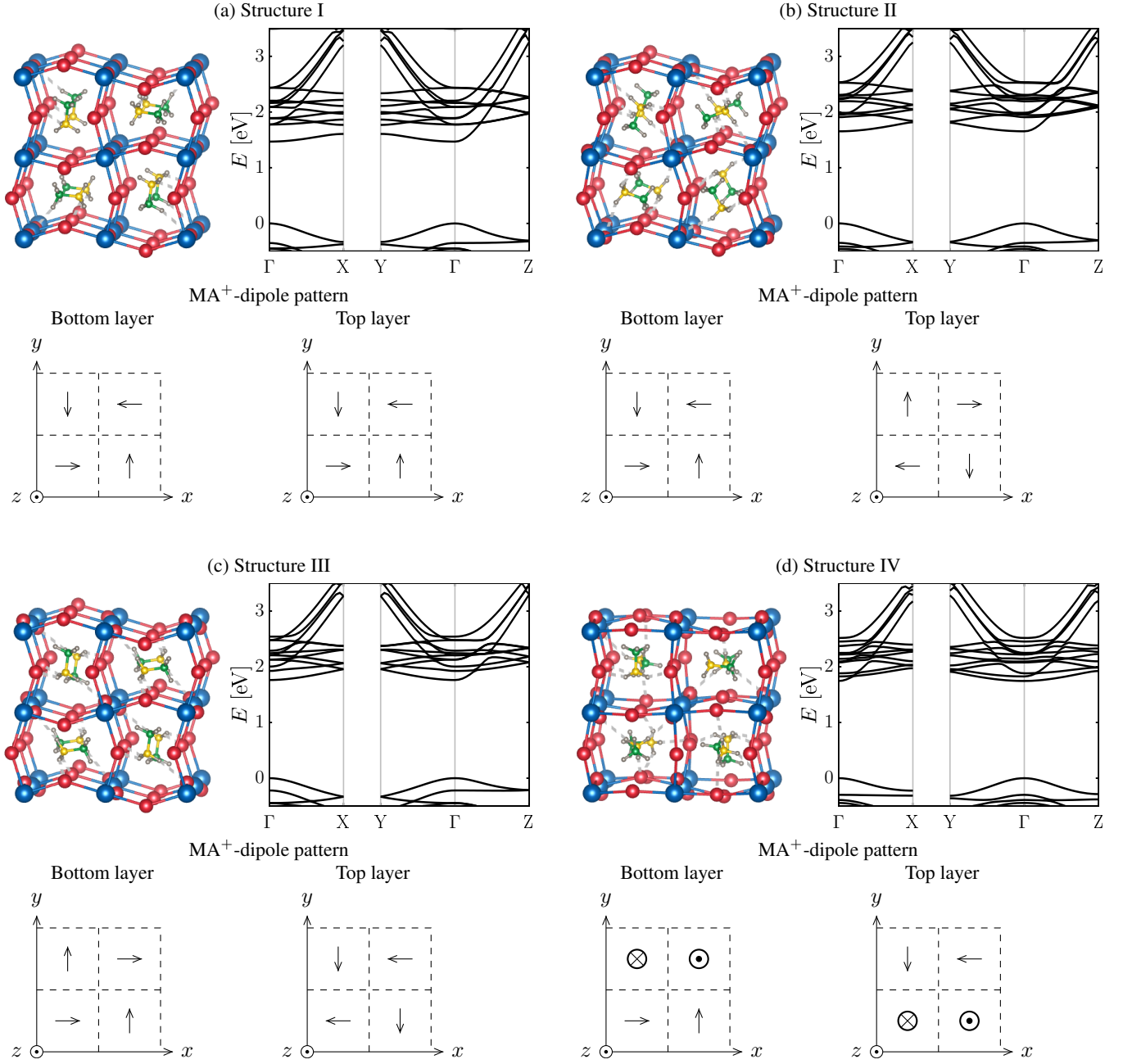


Figure 5. Four optimized  $2 \times 2 \times 2$  supercell structures I, II, III and IV (in the upper-left panels) in which all MA<sup>+</sup> cations are oriented approximately face-to-face. For each system, the band structure (in the upper-right panel) as well as the patterns of MA<sup>+</sup> dipoles (in the lower panel) in the bottom ( $0 < z < 0.5$ ) and top ( $0.5 < z < 1$ ) layers of the unit cell (bottom panels) are also shown.

each system, the band structures in the  $\Gamma$ -X and  $\Gamma$ -Y directions are identical, while  $\Gamma$ -Z shows a different band dispersion.

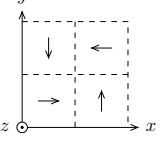
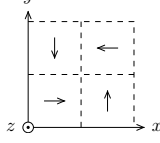
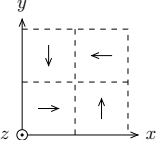
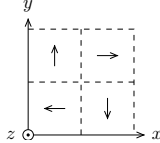
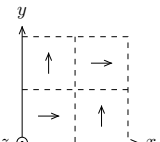
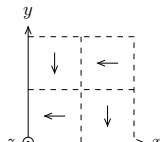
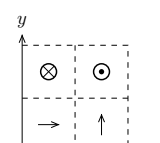
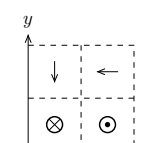
Conversely, in structure IV the MA<sup>+</sup> dipoles are oriented along the six different face-to-face directions  $\pm x$ ,  $\pm y$  and  $\pm z$ . The MA<sup>+</sup> alignment exhibits a quasi-random character and no equivalence between any two directions can be observed. This results in different lattice parameters  $a$ ,  $b$  and  $c$ . However, the root-mean-square deviation of  $\{a, b, c\}$  of structure IV is 0.13 Å, clearly smaller than structure I (0.19 Å), II (0.22 Å)

and III (0.18 Å). In addition, Fig. 5(d) shows that the band structures of structure IV along  $\Gamma$ -X,  $\Gamma$ -Y and  $\Gamma$ -Z are generally similar.

## 2. Pair-mode analysis

In the previous section, we discussed the lattice parameters and band structures of four characteristic  $2 \times 2 \times 2$  supercell models in terms of their dipole distribution. Now we analyze

Table I. Geometry parameters and properties of PBE+vdW optimized  $2 \times 2 \times 2$  supercell structures I, II, III and IV. Listed are lattice parameters (in Å), average  $\text{MA}^+$  dipole moment (in  $p_0$ ), patterns of  $\text{MA}^+$  dipoles in the unit cell, distribution of  $\text{MA}^+$ -dipole directions, pair-mode distribution, relative total energy (in meV per unit  $\text{MAPbI}_3$ ) and band gap (in eV).

Structure	Lattice parameters	Average $\text{MA}^+$ dipole moment	Bottom-layer pattern	Top-layer pattern	Dipole-direction distribution	Pair-mode distribution	Relative total energy	Band gap
I	$a = 12.28$ $b = 12.28$ $c = 12.68$	$ p_x  = 0.003$ $ p_y  = 0.000$ $ p_z  = 0.195$			$2+x, 2-x,$ $2+y, 2-y$	8 modes No. 20, 8 modes No. 22, 8 modes No. 23	112	1.469
II	$a = 12.26$ $b = 12.24$ $c = 12.71$	$ p_x  = 0.001$ $ p_y  = 0.002$ $ p_z  = 0.008$			$2+x, 2-x,$ $2+y, 2-y$	8 modes No. 20, 8 modes No. 22, 8 modes No. 24	23	1.654
III	$a = 12.24$ $b = 12.24$ $c = 12.62$	$ p_x  = 0.001$ $ p_y  = 0.000$ $ p_z  = 0.008$			$2+x, 2-x,$ $2+y, 2-y$	8 modes No. 20, 8 modes No. 22, 8 modes No. 24	0	1.762
IV	$a = 12.55$ $b = 12.24$ $c = 12.38$	$ p_x  = 0.003$ $ p_y  = 0.017$ $ p_z  = 0.012$			$1+x, 1-x,$ $1+y, 1-y,$ $2+z, 2-z$	8 modes No. 20, 8 modes No. 22, 4 modes No. 24, 4 modes No. 25	63	1.745

their total energies and band gaps in terms of pair modes. Figure 5 shows the dipole pattern for each geometry in the notation established in Fig. 1 (also listed in columns four and five of Table II).

For a  $2 \times 2 \times 2$  supercell model, each  $\text{MA}^+$  has 6 nearest neighbors, thus there are altogether  $\frac{1}{2} \cdot 8 \cdot 6 = 24$  pair modes after eliminating double counting. Since all dipoles in these four systems are oriented along face-to-face directions, only modes No. 18–25 will contribute. Specifically, in modes No. 18, 19 and 21, the two dipoles are (approximately) linearly aligned; modes No. 20 and 22 include two vertical dipoles; modes No. 23 and 24 two parallel dipoles; and the two dipoles in mode No. 25 are perpendicular to each other and not located in the same plane. These geometric characteristics are summarized in Table II.

In structure I, II or III, the orientation of dipoles within a layer (that is, with similar  $z$  coordinate) alternates between  $x$  and  $y$ . This results in 8 pair modes of type 20 and 8 modes of type 22 (these two different “vertical” modes, in which the two dipoles are vertical and approximately coplanar, appear in pairs due to the periodic boundary conditions for  $2 \times 2 \times 2$  supercell models). As a result, these three systems exhibit similar geometric properties as alluded to in the previous section.

However, both the total energy and band gap of structure I are significantly different from those of structures II and III, which we attribute to the difference in the remaining pair modes. In structures II and III, the dipoles in the “bottom” and the “top” layers are oriented in opposite directions, intro-

Table II. Relative geometry of dipoles in pair modes No. 18–25 defined in Fig. 2.

Mode No.	Dipole-dipole Geometry
18	linear, extending
19	linear, head-to-head
20	vertical
21	linear, tail-to-tail
22	vertical
23	parallel
24	antiparallel
25	out-of-plane

ducing 8 antiparallel modes (No. 24). This similarity leads to similar band gaps (difference  $\sim 0.1$  eV) and relatively close total energies (difference  $\sim 20$  meV per unit  $\text{MAPbI}_3$ ). In contrast, in structure I, the identical alignment in these two layers results in 8 parallel modes (No. 23). The significantly higher total energy ( $> 100$  meV per unit) suggests that mode No. 23, in which the two dipoles are aligned parallel, is less favorable than mode No. 24 that contains two antiparallel dipoles. In addition, the occurrence of the parallel mode also gives rise to a smaller band gap (by  $\sim 0.3$  eV compared to structure III). Our results for structures I–III suggest a correlation between the stability of hybrid perovskites and the size of the band gap, that is, the higher the stability the larger the band gap. This



observation agrees well with the trend reported by a recent experimental-theoretical study [55].

Despite the apparently different dipole-direction distribution, structure IV has a similar although not identical pair-mode distribution compared to structure III. The three-dimensional dipole-network results in 8 pair modes of type 20, 8 modes of type 22, 4 modes of type 24 and 4 modes of type 25. Hence, the major difference arises from the presence of mode No. 25, in which the two dipoles are approximately vertical and not located within the same plane. Our DFT results give a moderately higher total energy for structure IV ( $\sim 60$  meV per unit) and a band gap that is very close to that of structure III. This suggests that mode No. 25 does not significantly reduce the overall stability of the system.

Recapping the pair-mode distribution in  $2 \times 2 \times 2$  supercell models: The vertical modes, No. 20 and 22, are abundant. The antiparallel mode (No. 24) can significantly stabilize the system, whereas mode No. 25 decreases stability. The parallel mode (No. 23) is energetically unfavorable. The linear modes (No. 18, 19 and 21) are not present in structures I–IV.

### C. Pair-mode distribution in optimized $3 \times 3 \times 3$ supercell structures

In this section we discuss the DFT (PBE+vdW) results for a series of  $3 \times 3 \times 3$  MAPbI<sub>3</sub> supercell models. Our objective is to generate snapshots of the cubic (high-temperature) MAPbI<sub>3</sub> phase in which the MA<sup>+</sup> ions are disordered. We therefore fixed the lattice parameters to  $a = b = c = 18.94$  Å for the  $3 \times 3 \times 3$  supercells. This value corresponds to three times 6.31 Å — the experimental lattice parameter of the cubic-phase [7].

The atomic positions in the  $3 \times 3 \times 3$  supercell models were randomly initialized based on electrostatic considerations using the following protocol:

- (i) The MA<sup>+</sup> ions were approximated by the dipoles defined in Figs. 1(b) and (c). These dipoles were randomly selected and located at the centre of the single unit cells that make up the  $3 \times 3 \times 3$  supercell, thus forming different MA<sup>+</sup>-dipole alignments that reflect the disordered structures.
- (ii) The total electrostatic dipole-dipole interaction energy,  $E_{dd}$ , of the dipole configuration was calculated by summing the interaction energy of each dipole pair. We used  $p_0 = 2.2$  D and a dielectric constant of 25.7 [48] in this paper. The electrostatic energy is fast to compute and allows us to sample many thousands of  $3 \times 3 \times 3$  models to generate an energy distribution as shown in Fig. 6. The  $E_{dd}$ -distribution exhibits a Gaussian character centered at 0 meV.
- (iii) We then select individual samples from this energy distribution and used them as initial geometries for DFT structure optimization by converting the stylized dipoles back to atomic geometries.

From altogether 100 000 samples included in Fig. 6, we randomly picked 20 with a negative total electrostatic energy

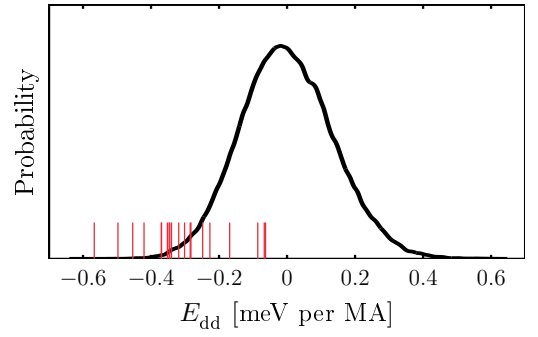


Figure 6. Probability-distribution of the electrostatic dipole-dipole interaction energy (per MA<sup>+</sup>-dipole) in  $3 \times 3 \times 3$  supercell models (black curve). The energies at which we picked the samples to initialize model systems for DFT calculations are indicated by the red vertical lines.

and converted them into initial structures of  $3 \times 3 \times 3$  supercell models for DFT calculations. In this paper, we applied an energy-dependent weighting factor in the selection, so that alignments with lower electrostatic energy had higher chance to be included (cf. the red lines' positions in Fig. 6). There are a considerable amount of diagonally-oriented MA<sup>+</sup>-dipoles in the initial structure, but most of them were reoriented into face-to-face directions in the DFT-optimized structures. Figure 7 shows an example: in this sample, there are 8 diagonal MA<sup>+</sup>-dipoles in the initial structure but 0 in the optimized structure. In addition, some MA<sup>+</sup>-dipoles that were initially oriented along face-to-face were reoriented, too.

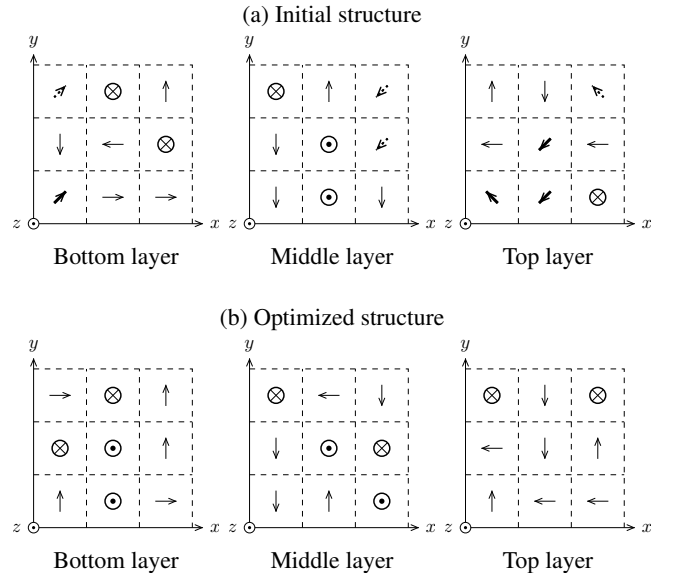


Figure 7. Dipole patterns of the bottom, middle and top layers of (a) the initial structure, and (b) the DFT-optimized structure of a  $3 \times 3 \times 3$  supercell sample.

In the optimized structures of all samples, the small average dipole moments (data not shown) indicates that they can be considered approximately nonpolar. Figures 8(a) and (b) show the optimized structures that have the highest and lowest

total energies among the 20 samples. Their difference is only 15 meV per unit  $\text{MAPbI}_3$ , which is very small compared to the total-energy difference among the  $2 \times 2 \times 2$  supercell models

discussed in the previous section. For comparison, the electrostatic dipole-dipole interaction energy difference between these two optimized structures is 0.02 meV per  $\text{MAPbI}_3$  unit.

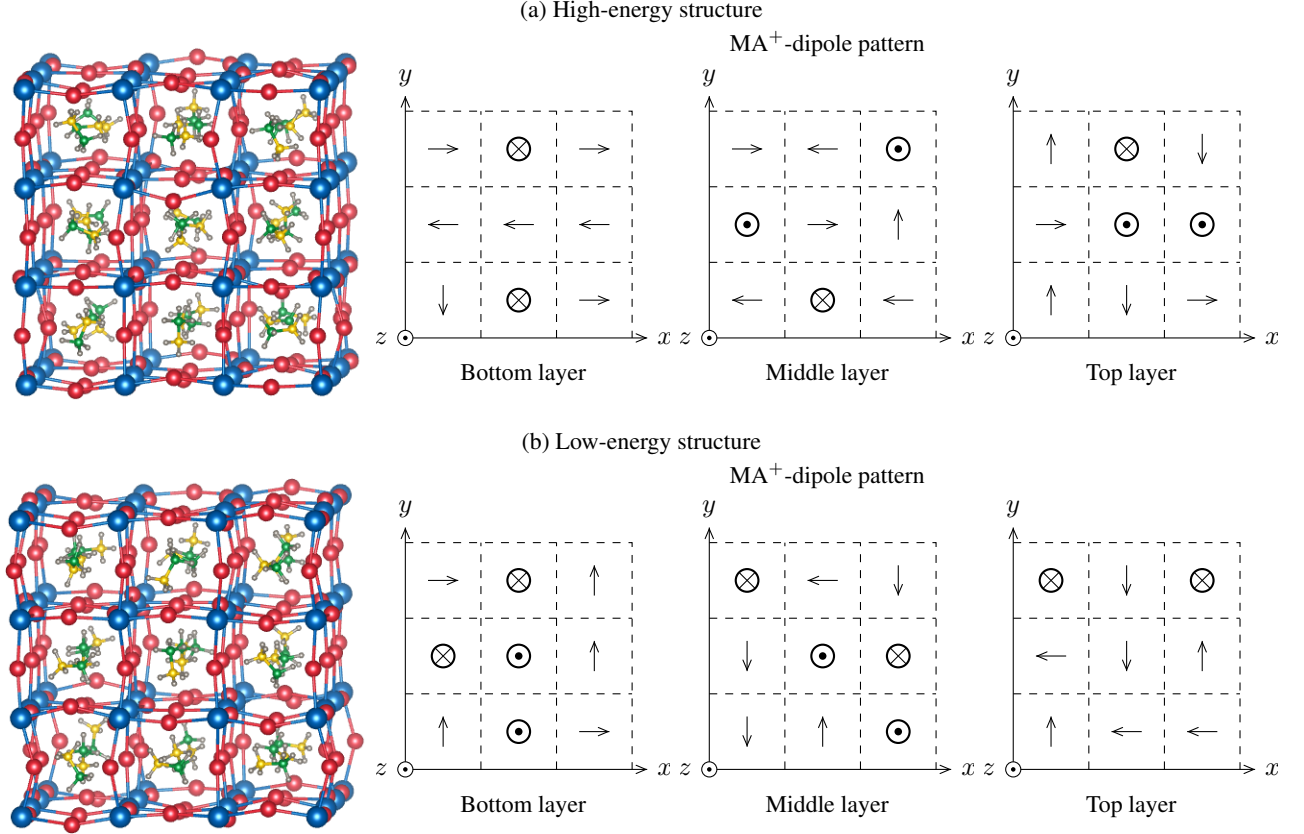


Figure 8. Two optimized structures of  $3 \times 3 \times 3$  supercell models as well as their dipole patterns of the bottom, middle and top layers.

Figure 8 depicts the dipole patterns of the bottom ( $0 < z < 0.33$ ), middle ( $0.33 < z < 0.67$ ) and top ( $0.67 < z < 1$ ) layers of both structures. The dipoles are distributed over all six face-to-face directions  $\pm x$ ,  $\pm y$  and  $\pm z$ , similar to structure IV of  $2 \times 2 \times 2$  supercell model discussed previously. Pair modes of type 20, 22, 24 and 25 dominate in both structures. Mode No. 18, in which two dipoles are oriented along the same face-to-face direction (quasi-)linearly, is also significantly populated. This mode effectively “extends” one face-to-face dipole into two, forming a domain along this direction. To quantify the pair-mode pattern, we generate a pair-mode distribution from the 20 considered samples in this work.

Figure 9(a) shows the pair-mode distribution of each sample as a heat map, and Fig. 9(b) shows the overall pair-mode distribution of all 20 samples (altogether  $20 \cdot \frac{1}{2} \cdot 27 \cdot 6 = 1620$  modes). Figure 9(a) indicates that the pair-mode distributions associated with all samples are similar. In general, the planar vertical modes, No. 20 and 22, as well as mode No. 25, are the most dominant. The antiparallel mode (No. 24) is also significantly populated. There is also noticeable probability to find the linearly extended mode (No. 18) and the parallel mode (No. 23). In contrast, the population of all pair modes that involve one or two diagonal dipoles, that is, No. 1–17, as well as the head-to-head (No. 19) and tail-to-tail (No. 21)

linear modes, is negligible.

How can we understand the pair-mode distribution shown in Fig. 9? To simplify our discussion, we only focus on the modes No. 18–25. For an arbitrary face-to-face dipole, the possibilities to construct different pair modes with another face-to-face nearest neighbor are different. For example, there are 2 ways to construct mode No. 18 [Fig. 10(a)] and 4 ways for No. 24 [Fig. 10(b)]. Table III lists the number of possibilities and their theoretical probability (i.e., number of possibilities divided by 36). We call this probability *theoretical*, because it refers to a system in which the dipoles are not interacting with each other (that is, neither electrostatically nor via cage deformation). From the DFT results, we can then extract the *actual probabilities* associated with these modes that take the full electrostatic and structural response into account. We define the *actual probability* as the number of times a mode occurs in the 20 samples divided by the total number of modes in the  $3 \times 3 \times 3$  supercell model (i.e., 1620). The resulting probabilities are also listed in Table III and enable a direct comparison between electrostatically non-interacting dipoles and the real systems.

We start from the three most populated modes. Table III indicates that the theoretical and actual probabilities are very close for both vertical modes, No. 20 and 22. They can be



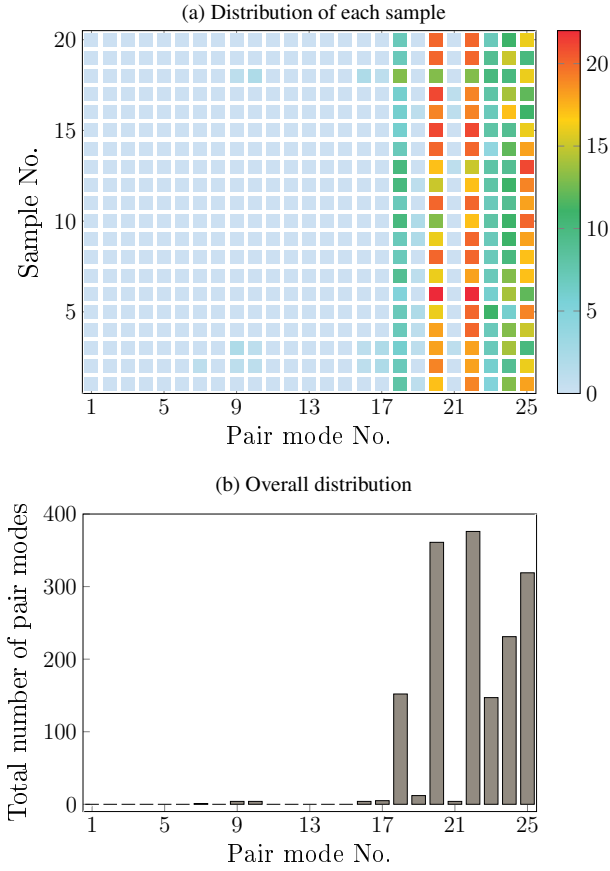


Figure 9. Pair-mode distribution of optimized  $3 \times 3 \times 3$  supercell models: (a) distribution of each individual sample, and (b) the overall distribution of all samples.

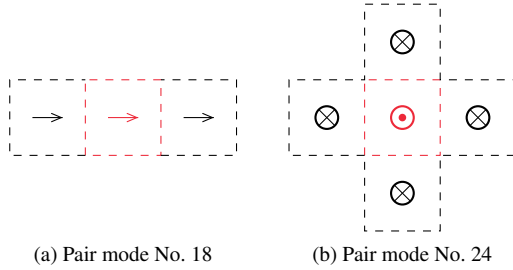


Figure 10. Possibilities to construct pair mode (a) No. 18 and (b) No. 24 for a face-to-face dipole (colored in red) with its nearest neighbors (colored in black).

understood as “intrinsically” dominant modes. A noticeable drop (0.025, namely 11.4%) can be observed in the DFT results for the out-of-plane mode (No. 25). Within the least populated linear modes, the comparison between the probabilities in non-interacting systems and actual probabilities are different. The  $\text{MA}^+$ -pair interaction results in a 0.046 (82.2%) total drop for both the head-to-head mode (No. 19) and the tail-to-tail mode (No. 21), while an increase of 0.038 (68.9%) is observed for the extending mode (No. 18). Finally, the populations of the parallel mode (No. 23) and the antiparallel mode

Table III. Number of possibilities and theoretical (non-interacting) probability to construct a pair mode (from No. 18 to No. 25) for an arbitrary face-to-face dipole, as well as the actual probability of this mode in the 20 investigated  $3 \times 3 \times 3$  supercell-models.

Mode No.	Number of possibilities	Probability in non-interacting systems	Actual probability
18	2	0.056	0.094
19	1	0.028	0.007
20	8	0.222	0.223
21	1	0.028	0.002
22	8	0.222	0.232
23	4	0.111	0.091
24	4	0.111	0.143
25	8	0.222	0.197

(No. 24) in optimized structures are 0.020 (18.3%) lower and 0.031 (28.3%) higher than the theoretical values, respectively.

This comparison indicates that, in  $\text{MAPbI}_3$ , the interaction between the neighboring  $\text{MA}^+$  ions significantly favors mode No. 18, which creates a linear alignment of dipoles that will be advantageous for charge transport. Conversely, the population-increase in mode No. 24 and decrease in mode No. 23 will oppose linear domain formation. Overall this will result in the following domain structure: a linear domain is adjacent to another linear domain containing electric dipoles oriented along the opposite direction. These findings qualitatively agree with the previous Monte Carlo simulations at 300 K that was based on *ab initio* MD and employed a classical Hamiltonian to describe the dynamic motion of dipoles [29]. However, on average we expect a domain size (length) smaller than that was reported in Ref. [29]. The origin is the prevalent population of the vertical modes No. 20 and 22, by which a domain is terminated. This discrepancy arises because the MD-based Monte Carlo simulations in Ref. [29] (i) were performed for a two-dimensional model and thereby neglect the interaction with the third dimension completely, and (ii) only included the direct (electrostatic) interaction between dipoles, while our DFT calculations also include the indirect interaction via the deformation of the inorganic cage.

The pair-mode distribution shown in Fig. 9 enables us to construct larger  $\text{MAPbI}_3$  models that are out of reach of DFT. As an example, Fig. 11 shows the  $\text{MA}^+$ -alignment in a layer of the thus-constructed  $20 \times 20 \times 20$  supercell. This  $20 \times 20 \times 20$  model was generated iteratively, applying the pair-mode distribution shown in Fig. 9. Details of the construction and an analysis of the results will be presented in a future publication. Since these large-scale models follow the  $\text{MA}^+$ -distribution of stable orientations and include  $\text{MA}^+$  nearest-neighbor interactions, they provide good models to study realistic  $\text{MAPbI}_3$  structures under realistic conditions.

The improvement of Fig. 9 and the multiscale modeling of these large  $\text{MAPbI}_3$  models are the subjects of future work.

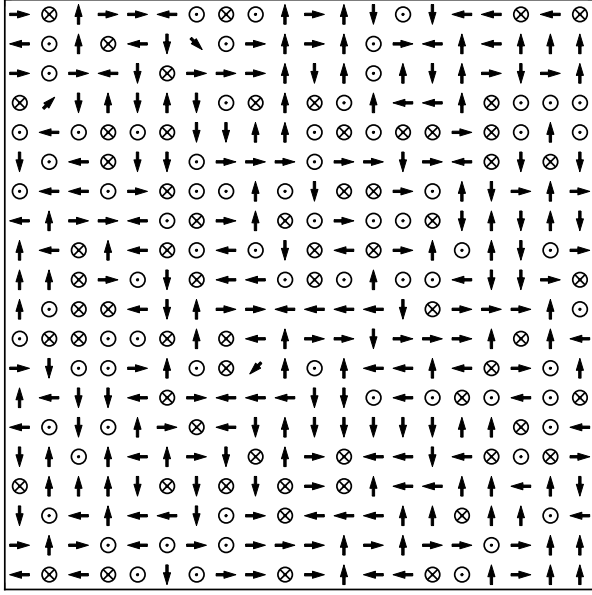


Figure 11. The alignment of  $\text{MA}^+$  dipoles in a layer of a  $20 \times 20 \times 20$  supercell.

#### IV. CONCLUSIONS

We have studied a series of  $\text{MAPbI}_3$  supercell models using DFT. To establish a multiscale model, we derived and analyzed the concept of “pair modes”, i.e., the interaction of nearest  $\text{MA}^+$ -ion pairs. We first investigated several small  $2 \times 2 \times 2$  supercell models, in which we can cancel out the

overall dipole moment by hand using suitable dipole orientations. Our DFT results indicate that differences in pair modes have a significant effect on the atomic and electronic structure of these models. This finding motivated our exploration into larger  $3 \times 3 \times 3$   $\text{MAPbI}_3$  supercell models, which we used to simulate disordered  $\text{MAPbI}_3$  structures by randomly initializing the  $\text{MA}^+$  orientations. Structural optimization using DFT and our pair mode analysis reveal that the final locations of  $\text{MA}^+$  ions is not fully random, but follows certain preferred orientations that depend on the surrounding. We use this dipole distribution to build up a multiscale model to generate the local structure in bulk  $\text{MAPbI}_3$  samples on large length scales, e.g., of a few tens of single cells.

#### ACKNOWLEDGMENT

We thank H. Levard for fruitful discussions. The generous allocation of computing resources by the CSC-IT Center for Science (via the Project No. ay6311) and the Aalto Science-IT project are gratefully acknowledged. An award of computer time was provided by the Innovative and Novel Computational Impact on Theory and Experiment (INCITE) program. This research used resources of the Argonne Leadership Computing Facility, which is a DOE Office of Science User Facility supported under Contract DE-AC02-06CH11357. This work was supported by the Academy of Finland through its Centres of Excellence Programme (2012-2014 and 2015-2017) under project numbers 251748 and 284621, as well as its Key Project Funding scheme under project number 305632.

- 
- [1] H. J. Snaith, *J. Phys. Chem. Lett.* **4**, 3623 (2013).
  - [2] M. A. Green, A. Ho-Baillie, and H. J. Snaith, *Nature Photon.* **8**, 506 (2014).
  - [3] <https://www.nrel.gov/pv/assets/images/efficiency-chart.png> (National Renewable Energy Laboratory: Best research-cell efficiencies, 2016).
  - [4] H.-S. Kim, C.-R. Lee, J.-H. Im, K.-B. Lee, T. Moehl, A. Marchioro, S.-J. Moon, R. Humphry-Baker, J.-H. Yum, J. E. Moser, et al., *Sci. Rep.* **2**, 591 (2012).
  - [5] M. M. Lee, J. Teuscher, T. Miyasaka, T. N. Murakami, and H. J. Snaith, *Science* **338**, 643 (2012).
  - [6] P. Jackson, R. Wuerz, D. Hariskos, E. Lotter, W. Witte, and M. Powalla, *Phys. Status Solidi Rapid Res. Lett.* **10**, 583 (2016).
  - [7] C. C. Stoumpos, C. D. Malliakas, and M. G. Kanatzidis, *Inorg. Chem.* **52**, 9019 (2013).
  - [8] S. de Wolf, J. Holovsky, S.-J. Moon, P. Löper, B. Niesen, M. Ledinsky, F.-J. Haug, J.-H. Yum, and C. Ballif, *J. Phys. Chem. Lett.* **5**, 1035 (2014).
  - [9] S. D. Stranks, G. E. Eperon, G. Grancini, C. Menelaou, M. J. P. Alcocer, T. Leijtens, L. M. Herz, A. Petrozza, and H. J. Snaith, *Science* **342**, 341 (2013).
  - [10] G. Xing, N. Mathews, S. Sun, S. S. Lim, Y. M. Lam, M. Grätzel, S. Mhaisalkar, and T. C. Sum, *Science* **342**, 344 (2013).
  - [11] C. S. Ponseca, Jr., T. J. Savenije, M. Abdellah, K. Zheng, A. Yartsev, T. Pascher, T. Harlang, P. Chabera, T. Pullerits, A. Stepanov, et al., *J. Am. Chem. Soc.* **136**, 5189 (2014).
  - [12] M. B. Johnston and L. M. Herz, *Acc. Chem. Res.* **49**, 146 (2016).
  - [13] H. J. Snaith, A. Abate, J. M. Ball, G. E. Eperon, T. Leijtens, N. K. Noel, S. D. Stanks, J. T.-W. Wang, K. Wojciechowski, and W. Zhang, *J. Phys. Chem. Lett.* **5**, 1511 (2014).
  - [14] H.-S. Kim, I.-H. Jand, N.-Y. Ahn, M.-S. Choi, A. Guerrero, J. Bisquert, and N.-G. Park, *J. Phys. Chem. Lett.* **6**, 4633 (2015).
  - [15] B. Chen, M. Yang, S. Priya, and K. Zhu, *J. Phys. Chem. Lett.* **7**, 905 (2016).
  - [16] J.-H. Noh, S.-H. Im, J.-H. Heo, T. N. Mandal, and S.-I. Seok, *Nano Lett.* **13**, 1764 (2013).
  - [17] G. Niu, W. Li, F. Meng, L. Wang, H. Dong, and Y. Qiu, *J. Mater. Chem. A* **2**, 705 (2014).
  - [18] G. Niu, X. Guo, and L. Wang, *J. Mater. Chem. A* **3**, 8970 (2015).
  - [19] A. Poglitsch and D. Weber, *J. Chem. Phys.* **87**, 6373 (1987).
  - [20] M. T. Weller, O. J. Weber, P. F. Henry, A. M. di Pompo, and T. C. Hansen, *Chem. Commun.* **51**, 4180 (2015).
  - [21] D. A. Egger, A. M. Rappe, and L. Kronik, *Acc. Chem. Res.* **49**, 573 (2016).
  - [22] N. Onoda-Yamamuro, T. Matsuo, and H. Suga, *J. Phys. Chem. Solids* **53**, 935 (1992).
  - [23] E. Mosconi, C. Quarti, T. Ivanovska, G. Ruani, and F. de Angelis, *Phys. Chem. Chem. Phys.* **16**, 16137 (2014).

- [24] J.-H. Lee, N. C. Bristowe, P. D. Bristowe, and A. K. Cheetham, *Chem. Commun.* **51**, 6434 (2015).
- [25] J. Li and P. Rinke, in preparation.
- [26] D. A. Egger and L. Kronik, *J. Phys. Chem. Lett.* **5**, 2728 (2014).
- [27] J. Li and P. Rinke, *Phys. Rev. B* **94**, 045201 (2016).
- [28] J. M. Frost, K. T. Butler, F. Brivio, C. H. Hendon, M. van Schilfgaarde, and A. Walsh, *Nano Lett.* **14**, 2584 (2014).
- [29] J. M. Frost, K. T. Butler, and A. Walsh, *APL Mater.* **2**, 081506 (2014).
- [30] A. M. A. Leguy, J. M. Frost, A. P. McMahon, V. Garcia Sakai, W. Kochelmann, C. H. Law, X. Li, F. Foglia, A. Walsh, B. C. O'Regan, et al., *Nature Comm.* **6**, 7124 (2015).
- [31] P. Umari, E. Mosconi, and F. de Angelis, *Sci. Rep.* **4**, 4467 (2014).
- [32] E. Menéndez-Proupin, P. Palacios, P. Wahnón, and J. C. Conesa, *Phys. Rev. B* **90**, 045207 (2014).
- [33] W. Yin, J. Yang, J.-G. Kang, Y. Yan, and S. Wei, *J. Mater. Chem. A* **3**, 8926 (2015).
- [34] F. Brivio, J. M. Frost, J. M. Skelton, A. J. Jackson, O. J. Weber, M. T. Weller, A. R. Goñi, A. M. A. Leguy, P. R. F. Barnes, and A. Walsh, *Phys. Rev. B* **92**, 144308 (2015).
- [35] I. Deretzis, B. N. di Mauro, A. Alberti, G. Pellegrino, E. Smecca, and A. la Magna, *Sci. Rep.* **6**, 24443 (2016).
- [36] W. Yin, T. Shi, and Y. Yan, *Appl. Phys. Lett.* **104**, 063903 (2014).
- [37] J.-S. Kim, S.-H. Lee, J.-H. Lee, and K.-H. Hong, *J. Phys. Chem. Lett.* **5**, 1312 (2014).
- [38] This is a short notation for simplicity and does not mean that we treat an  $\text{MA}^+$  ion only as a dipole.
- [39] J. Li, J. Järvi, and P. Rinke, in preparation.
- [40] J. P. Perdew, K. Burke, and M. Ernzerhof, *Phys. Rev. Lett.* **77**, 3865 (1996).
- [41] A. Tkatchenko and M. Scheffler, *Phys. Rev. Lett.* **102**, 073005 (2009).
- [42] E. van Lenthe, E. J. Baerends, and J. G. Snejders, *J. Chem. Phys.* **99**, 4597 (1993).
- [43] J. Even, L. Pedesseau, M.-A. Dupertuis, J.-M. Jancu, and C. Katan, *Phys. Rev. B* **86**, 205301 (2012).
- [44] J. Even, L. Pedesseau, J.-M. Jancu, and C. Katan, *J. Phys. Chem. Lett.* **4**, 2999 (2013).
- [45] F. Brivio, K. T. Butler, A. Walsh, and M. van Schilfgaarde, *Phys. Rev. B* **89**, 155204 (2014).
- [46] C. Katan, L. Pedesseau, M. Kepenekian, A. Rolland, and J. Even, *J. Mater. Chem. A* **3**, 9232 (2015).
- [47] F. Chiarella, A. Zappettini, F. Licci, I. Borriello, G. Cantele, D. Ninno, A. Cassinese, and R. Vaglio, *Phys. Rev. B* **77**, 045129 (2008).
- [48] F. Brivio, A. B. Walker, and A. Walsh, *APL Mater.* **1**, 042111 (2013).
- [49] V. Blum, R. Gehrke, F. Hanke, P. Havu, V. Havu, X. Ren, K. Reuter, and M. Scheffler, *Comput. Phys. Comm.* **180**, 2175 (2009).
- [50] V. Havu, V. Blum, P. Havu, and M. Scheffler, *J. Comput. Phys.* **228**, 8367 (2009).
- [51] S. V. Levchenko, X. Ren, J. Wierfink, R. Johanni, P. Rinke, V. Blum, and M. Scheffler, *Comput. Phys. Comm.* **192**, 60 (2015), ISSN 0010-4655.
- [52] F. Knuth, C. Carbogno, V. Atalla, V. Blum, and M. Scheffler, *Comput. Phys. Comm.* **190**, 33 (2015).
- [53] See <http://dx.doi.org/10.17172/NOMAD/2017.03.31-1>.
- [54] See Supplemental Material at <http://link.aps.org/> for individual  $\text{MA}^+$ -dipoles and pair modes including the deviation from face-to-face directions; structural parameters and band structures of several  $2 \times 2 \times 2$  supercells.
- [55] T. Baikie, Y. Fang, J. M. Kadro, M. Schreyer, F. Wei, S. G. Mhaisalkar, M. Grätzel, and T. J. White, *J. Mater. Chem. A* **1**, 5628 (2013).

Supplemental Material for

**Pair modes of organic cations in hybrid perovskites: Insight from first-principles calculations of supercell models**

Jingrui Li<sup>1,\*</sup>, Jari Järvi<sup>1,2</sup> and Patrick Rinke<sup>1</sup>

<sup>1</sup>*Centre of Excellence in Computational Nanoscience (COMP) and Department of Applied Physics,  
Aalto University, P.O.Box 11100, FI-00076 AALTO, Finland*

<sup>2</sup>*Department of Physics, University of Helsinki, P.O.Box 64, FI-00014 University of Helsinki, Finland*

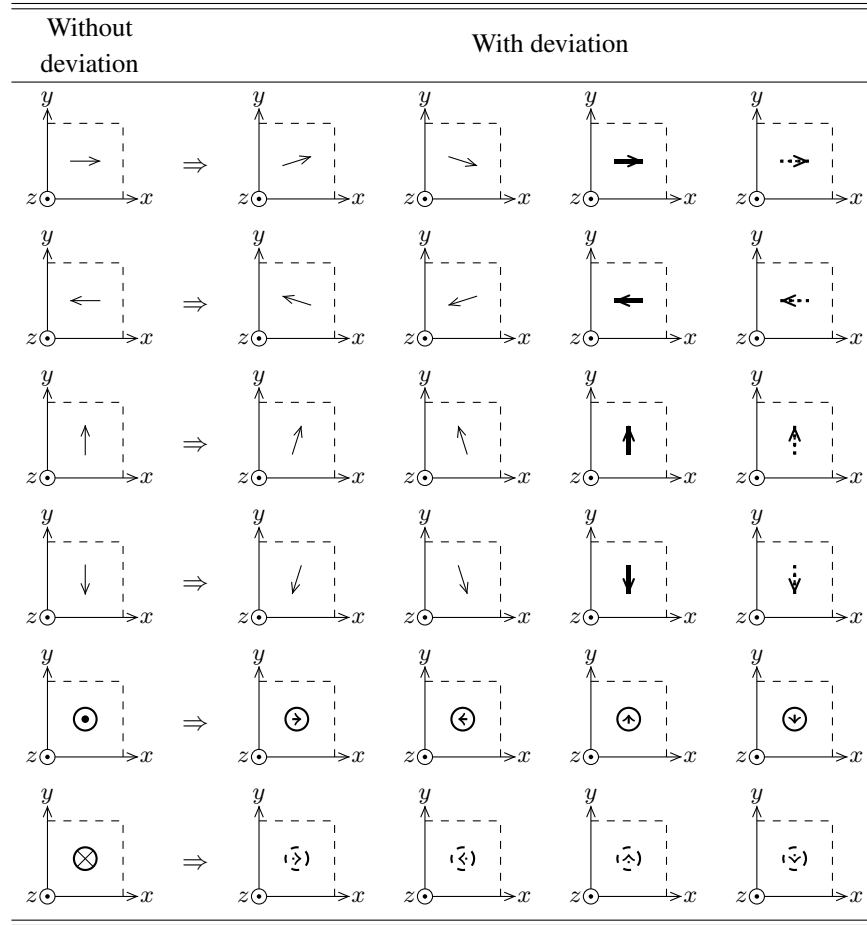
---

\*: jingrui.li@aalto.fi

# S1. PAIR-MODE DEFINITION WHEN CONSIDERING THE DEVIATION OF $\text{MA}^+$ -DIPOLES FROM THE FACE-TO-FACE DIRECTION

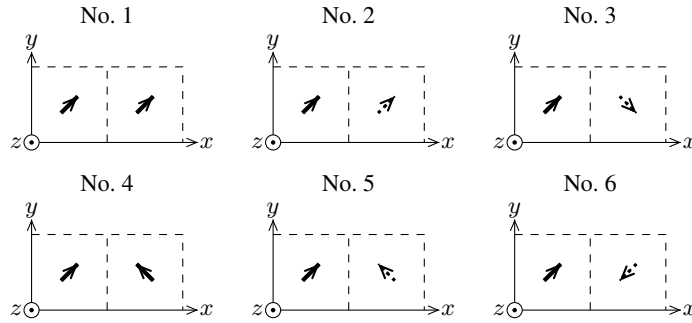
In our previous work [1] we found two stable orientations for  $\text{MA}^+$  cations in the cubic primitive-cell model. In the “diagonal” structure [the left structure of Fig. 1(a) in the manuscript], the C–N bond is oriented along the diagonal direction of the single unit cell. We thus denote the direction of the  $\text{MA}^+$ -dipole  $[111]$ ,  $[1\bar{1}\bar{1}]$ , and so forth. In the “face-to-face” structure [the right structure of Fig. 1(b) in the manuscript], the C–N bond is oriented along the face-to-face direction of the single unit cell with a small deviation. This deviation is system- and model-dependent. For example, it is  $23.2^\circ$  in the primitive-cell model of  $\text{MAPbI}_3$  [1],  $22.3^\circ$  on average in structure II, and  $8.4^\circ$  on average in Structure III. According to the primitive-cell results [1], the C–N bond along the  $[100]$  direction is located in the symmetry planes  $[002]$  or  $[020]$ . The resulting C–N bond directions including the deviation are then  $[1\epsilon 0]$ ,  $[1\bar{\epsilon} 0]$ ,  $[10\epsilon]$  or  $[10\bar{\epsilon}]$ .

The six face-to-face  $\text{MA}^+$  dipoles in Fig. 1(c) in the manuscript can be subdivided into twenty-four dipole directions as follows (thick solid and dashed arrows point out of and into the plane of the paper, respectively):

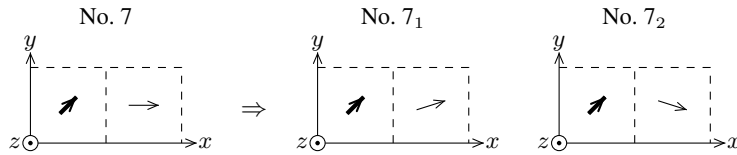


Together with the eight diagonal directions, there are 32 possible directions for an  $\text{MA}^+$  dipole. This results in 86 symmetry inequivalent modes as follows:

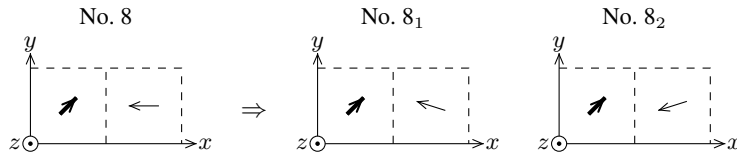
- Pair modes No. 1–6:



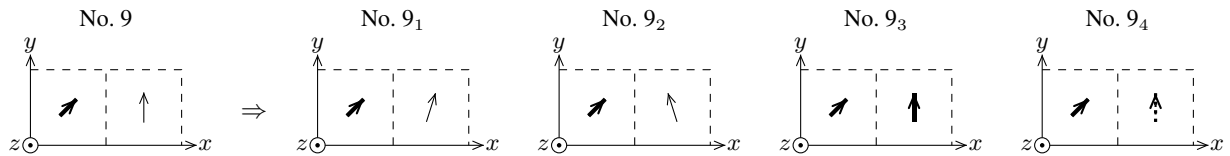
- Pair mode No. 7 can be split into 2 variations:



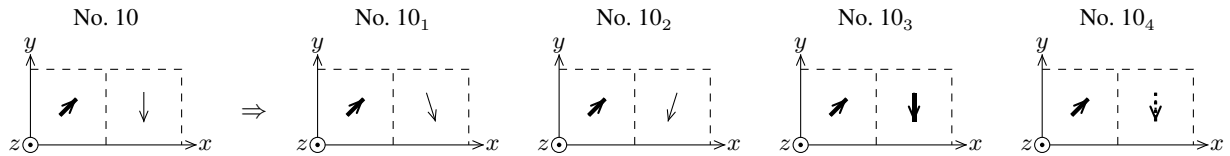
- Pair mode No. 8 splits into 2 variations:



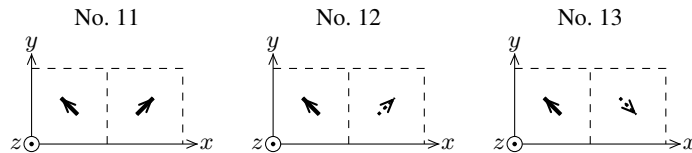
- Pair mode No. 9 splits into 4 variations:



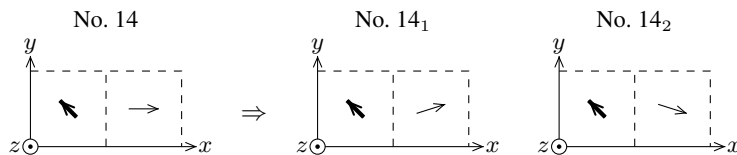
- Pair mode No. 10 splits into 4 variations:



- Pair modes No. 11–13:

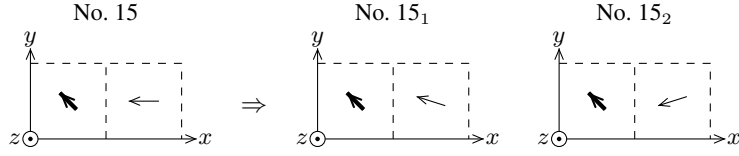


- Pair mode No. 14 splits into 2 variations:

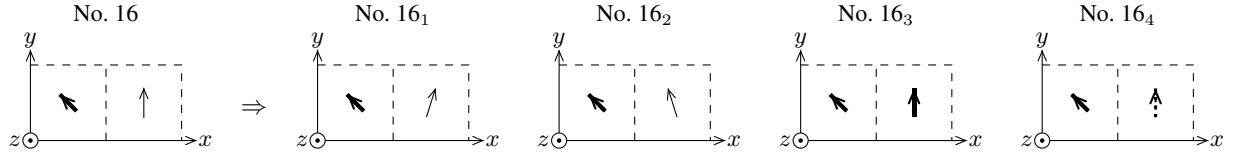




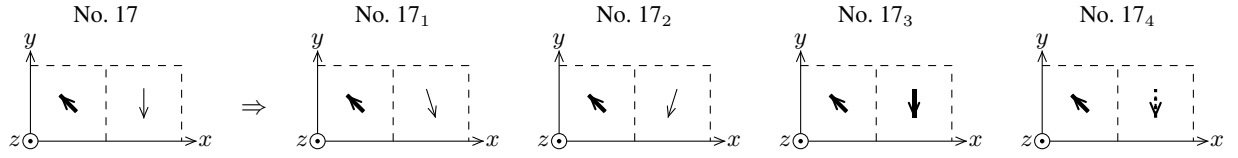
- Pair mode No. 15 splits into 2 variations:



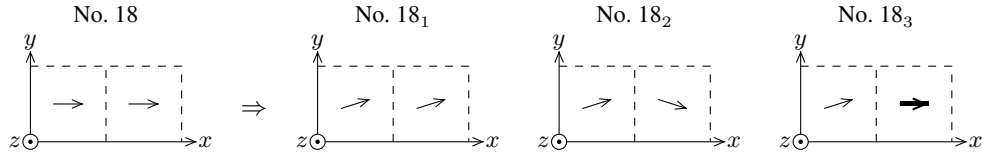
- Pair mode No. 16 splits into 4 variations:



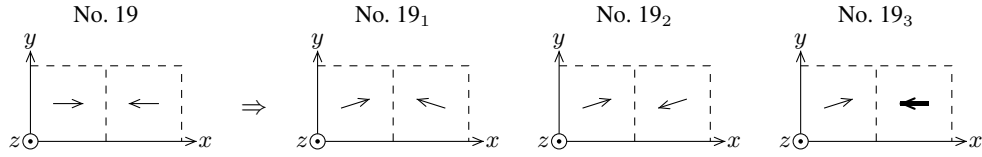
- Pair mode No. 17 splits into 4 variations:



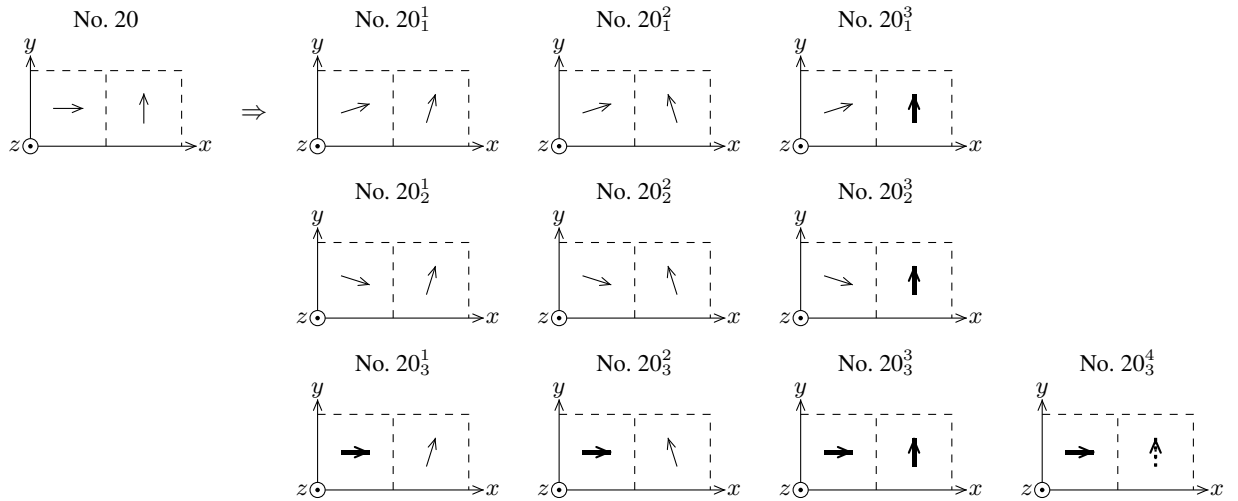
- Pair mode No. 18 splits into 3 variations:



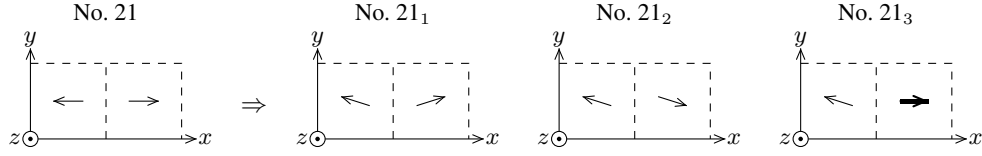
- Pair mode No. 19 splits into 3 variations:



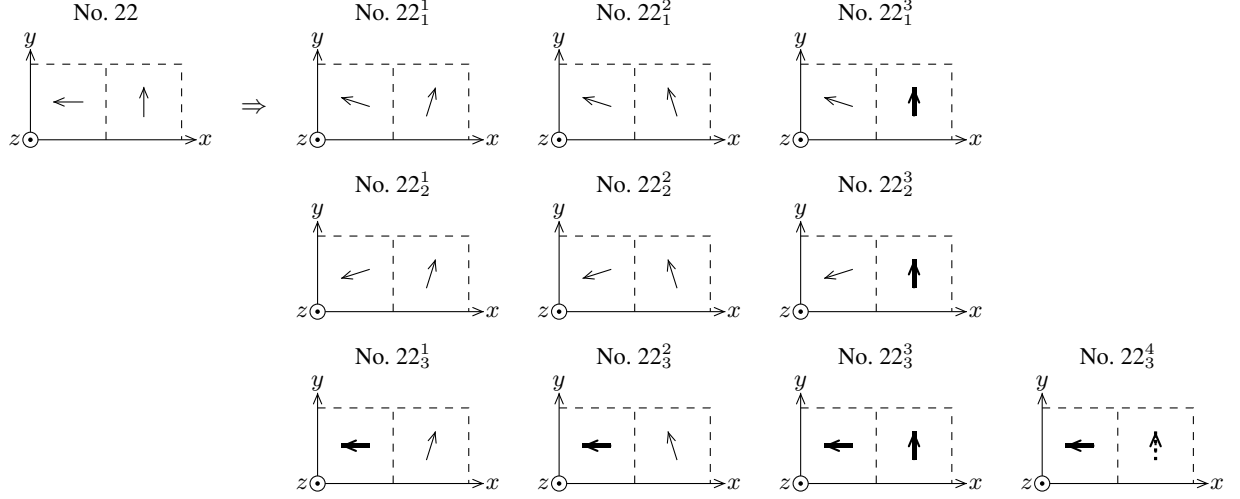
- Pair mode No. 20 splits into 10 variations:



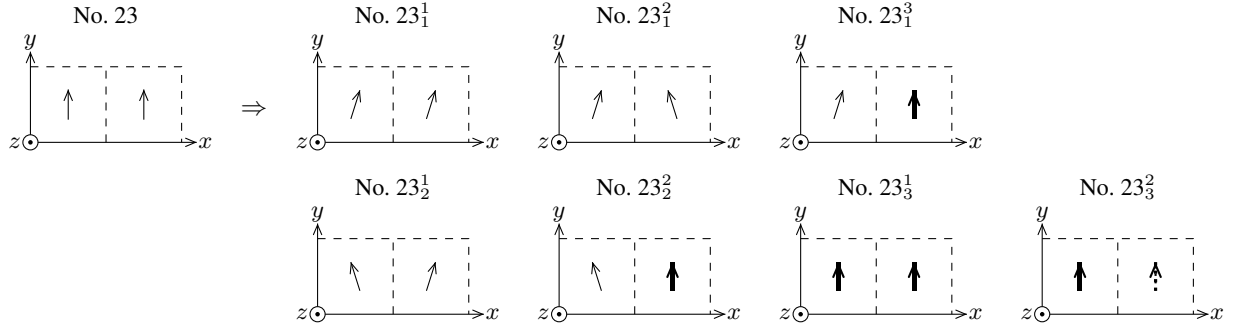
- Pair mode No. 21 splits into 3 variations:



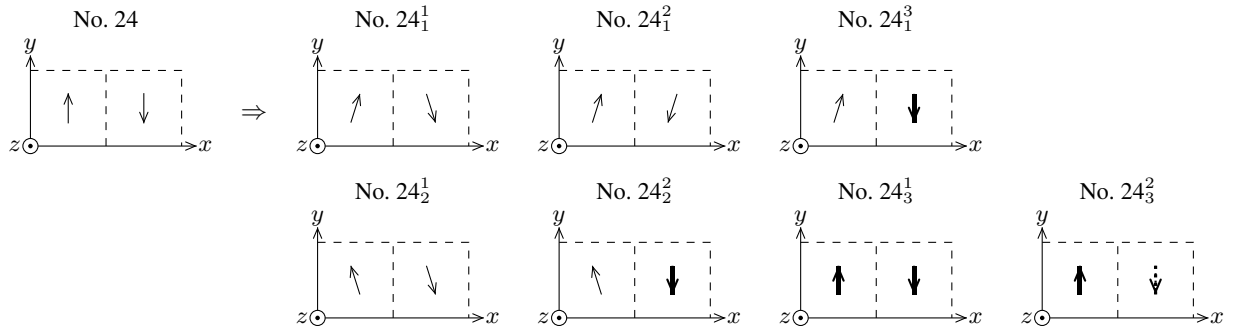
- Pair mode No. 22 splits into 10 variations:



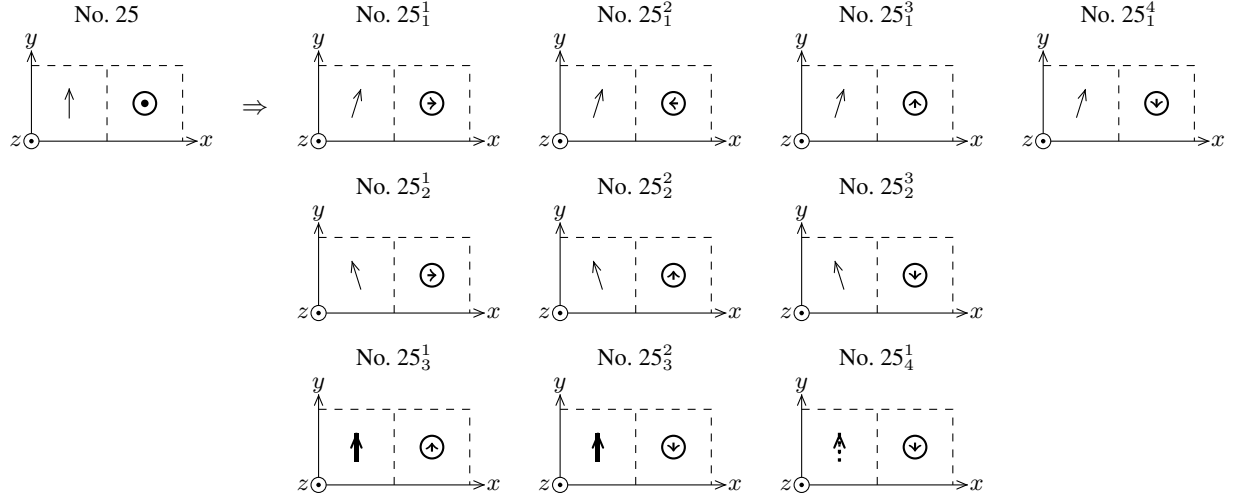
- Pair mode No. 23 splits into 7 variations:



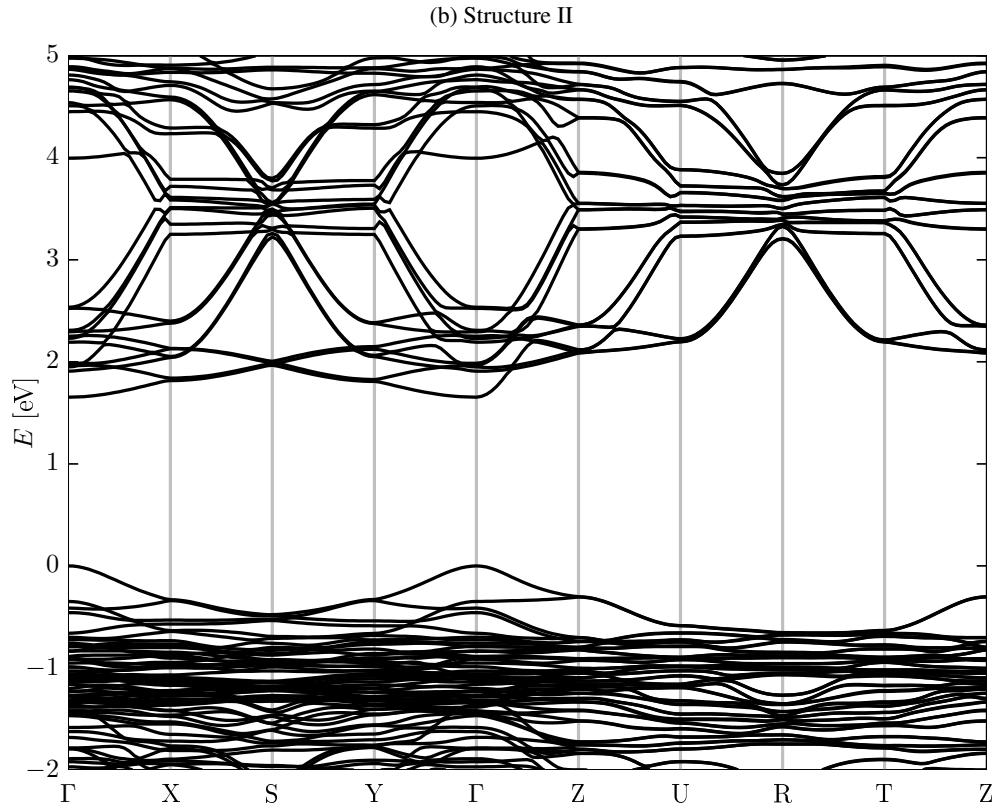
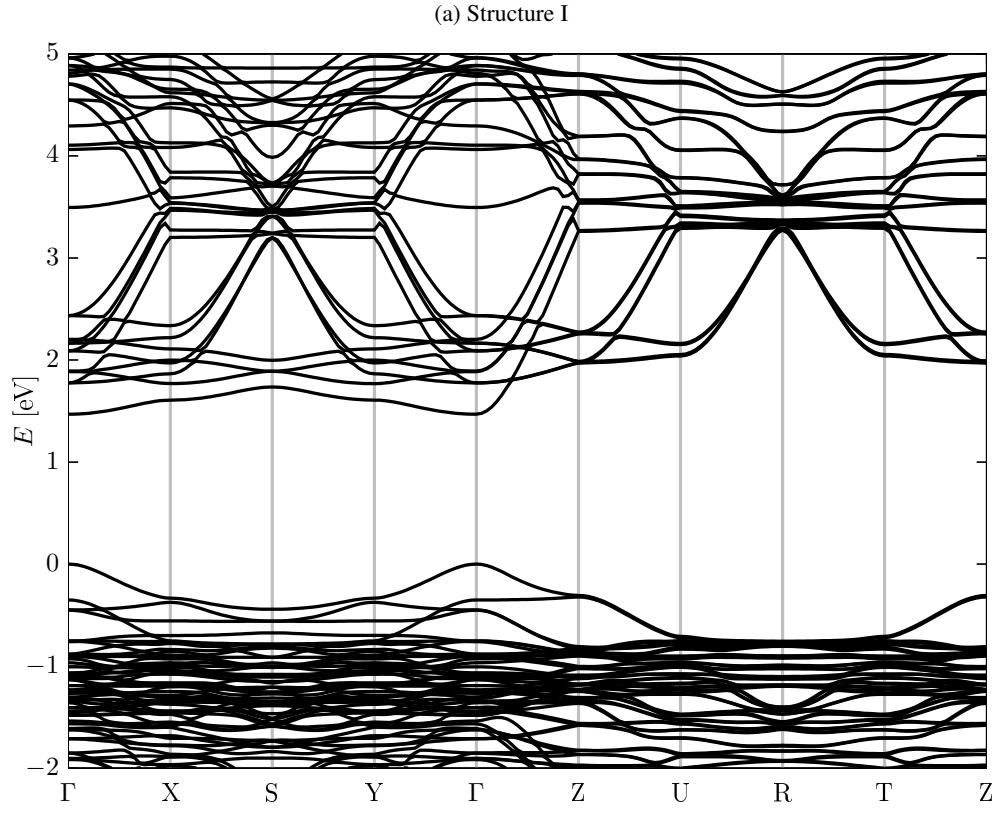
- Pair mode No. 24 splits into 7 variations:



- Pair mode No. 25 splits into 10 variations:



**S2. BAND STRUCTURE OF  $2 \times 2 \times 2$  SUPERCELL STRUCTURES I, II, III AND IV**



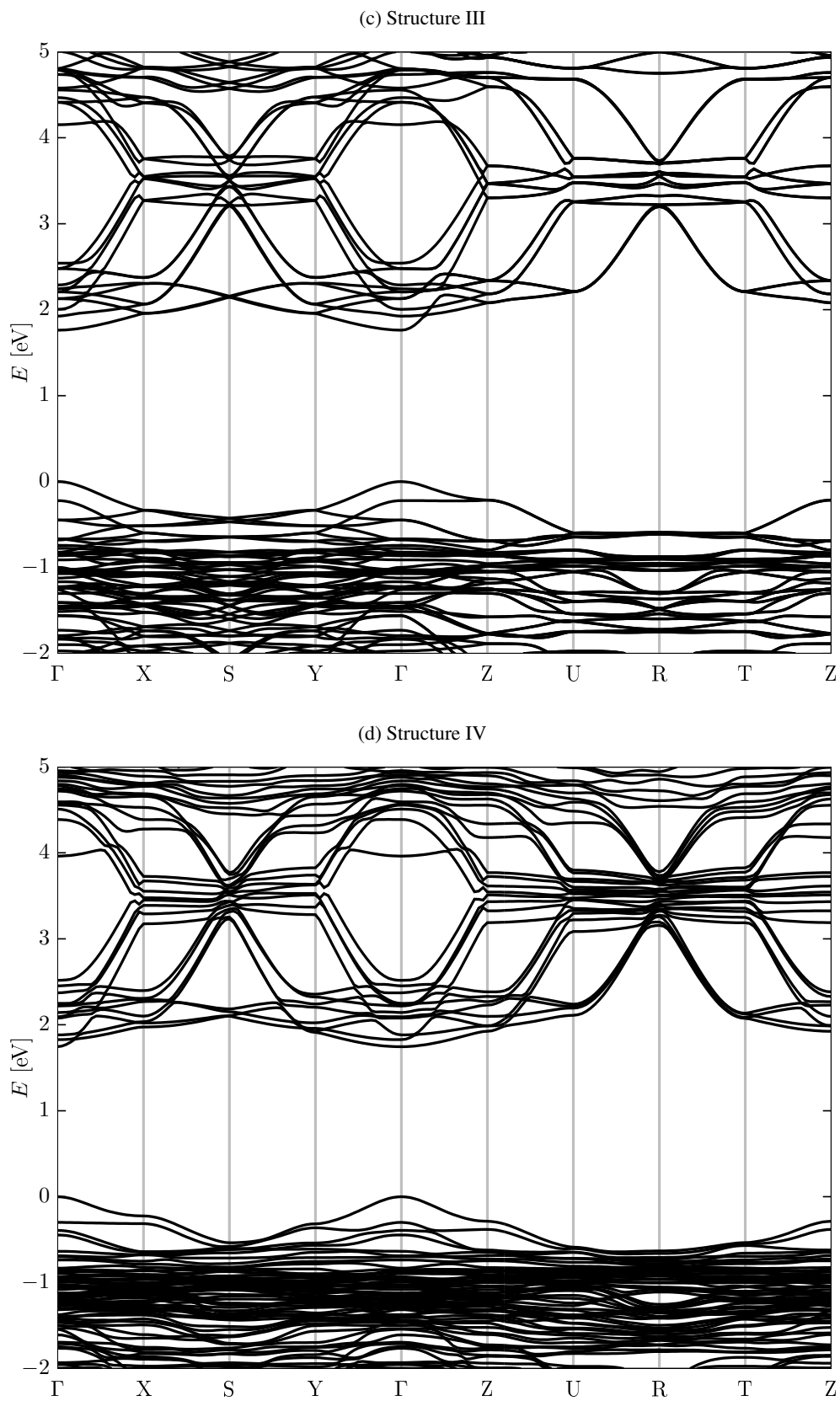


Figure S1. Band structures of the four optimized  $2 \times 2 \times 2$  supercell structures I, II, III and IV.

### S3. OPTIMIZED $2 \times 2 \times 2$ SUPERCELL STRUCTURE WITH ALL DIAGONALLY-ORIENTED $\text{MA}^+$ IONS

- Atomic structure: cf. Fig. 4 in the manuscript.
- Lattice parameters:  $a \approx b \approx c = 12.60 \text{ \AA}$ .
- Band structure (band gap = 1.347 eV):

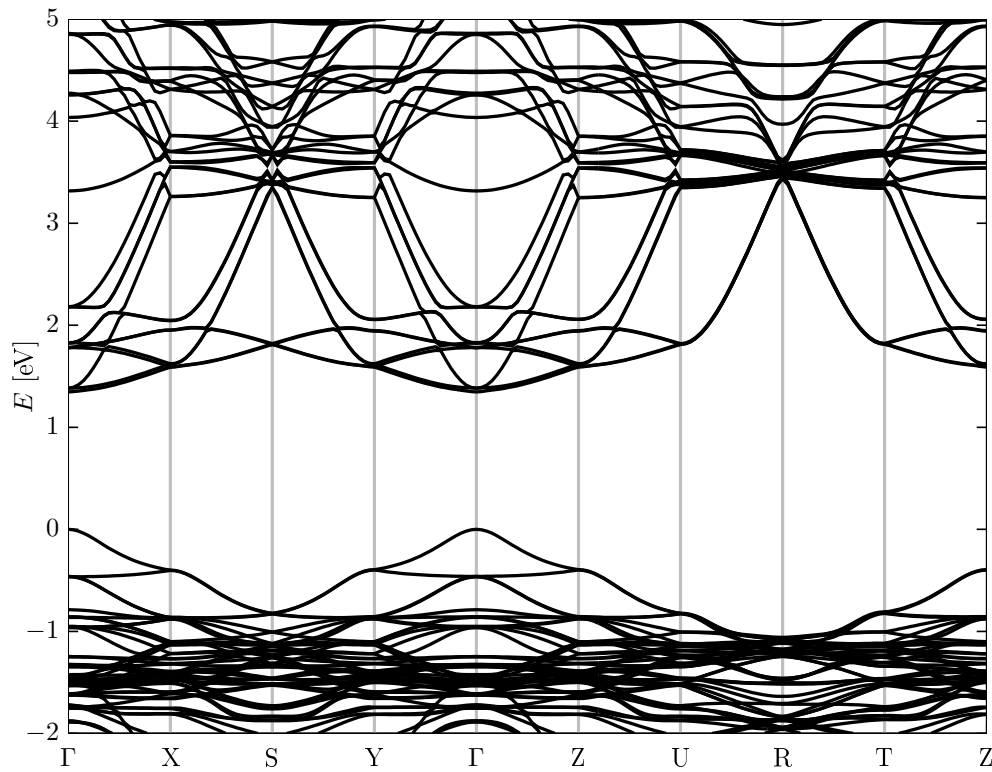


Figure S2. Band structure of the optimized  $2 \times 2 \times 2$  supercell structure in which all  $\text{MA}^+$  cations are oriented diagonally.